Structure and Crystallization Kinetics of as-deposited Films of the GeTe Phase Change Compound from Atomistic Simulations

*Simone Perego, Daniele Dragoni, Silvia Gabardi, Davide Campi, and Marco Bernasconi**

Address: Dipartimento di Scienza dei Materiali,
Università di Milano-Bicocca, Via R. Cozzi 55, I-20125 Milano, Italy
Email Address: *marco.bernasconi@unimib.it

Keywords: *Phase Change Materials, Molecular Dynamics Simulations, Machine Learning, Amorphous Materials*

Models of the amorphous phase of the GeTe compound have been generated by depositing individual atoms on a substrate by molecular dynamics simulations. This material is of interest for applications in phase change memories. The kinetic energy of the atoms impinging on the surface was in the range 1.5-10 eV which is typical of magnetron sputtering growth. The simulations with up to 8000 atoms exploit a machine learning potential devised previously by our group. The structural properties of the films depend very little on the energy of the impinging atoms in the range 1.5-10 eV and they are also very similar to those of amorphous models generated by quenching from the melt, but for a larger fraction of Ge-Ge bonds and Ge atoms in tetrahedral geometries in the films. We then simulated the crystal nucleation and growth at 600 K which is close to the temperature of maximal crystal growth velocity exploited in the memory devices. Despite the structural differences mentioned above, the kinetics of crystallization at 600 K is very similar for the as-deposited and melt-quenched amorphous models.

1 Introduction

Phase change chalcogenide alloys such as the flagship $Ge_2Sb_2Te_5$ (GST) compound are exploited in different electronic and optical devices thanks to their ability to undergo a fast and reversible transformation between the amorphous and crystalline phases upon heating [1, 2, 3, 4, 5, 6]. The large difference in electrical resistivity and optical reflectivity between the two phases allow encoding a binary information in electronic memories, named Phase Change Memory (PCM), and in optical disks (DVD, blu-ray disks) [1, 3]. Various on-chip photonic applications have also been realized by integrating phase change materials with optical waveguides [7, 8, 9]. The possibility to induce a partial crystallization of the amorphous phase with different levels of electrical resistivity is also exploited in neuromorphic electronic devices and in-memory computing [10].

In PCMs the amorphization of the crystal (RESET process) and the recrystallization of the amorphous phase (SET process) are induced by Joule heating via electrical pulses of different duration and intensity [2, 3]. The SET is the slow process of the memory which assigns the overall programming time. Large efforts have then been devoted in literature to study the kinetics of crystallization of phase change materials under different conditions [2, 11, 12, 13].

Phase change materials are typically deposited by sputtering in the amorphous phase which then turns into the crystalline phase by heating above the glass transition temperature T_g [14]. The reversible cycling between the crystalline and amorphous phases in the devices occur via melting of the crystal and amorphization by rapid quenching from the melt [2, 3].

There are several reports in literature showing that the crystallization process depends on the preparation conditions of the amorphous phase. Crystallization is much slower in the as-deposited (AD) amorphous films than in the melt-quenched (MQ) amorphous phase produced for instance by laser irradiation of the AD samples [15, 16, 17, 18]. The difference in the crystallization kinetics of AD and MQ samples is, however, dependent on the composition of the alloy. For the binary $GeTe_x$ alloys for instance, this difference is very striking for the eutectic composition $Ge_{15}Sb_{85}$ but it is less pronounced for the stoichiometric GeTe compound [17, 18]. For the ternary GST alloy, experiments on laser induced crystallization yielded an overall crystallization time of about 100 ns for AD samples and of less than 10 ns for the MQ samples [16]. This behavior was ascribed to the presence in MQ samples of a non-equilibrium distribution of quenched-in subcritical crystalline nuclei that reduces the incubation time for crystallization once the amorphous phase is brought above T_g [16]. The presence of quenched-in crystalline nuclei generated during the quenching was confirmed by fluctuation transmission electron microscopy in MQ samples generated by laser irradiation [19] or by Joule heating in a prototype PCM [20].

On the other hand, molecular dynamics (MD) simulations based on density functional theory (DFT) revealed some inherent differences in the structural properties of AD and MQ models of GST [21]. In general, the DFT models of the amorphous phase of GST generated by quenching from the melt display several different local environments [2, 22, 23]: Te atoms are mostly 3-fold coordinated in a pyramidal geometry, Sb atoms are both 3-fold coordinated in a pyramidal geometry and 4- or 5-fold coordinated in a defective octahedral environment (octahedral bonding angles but coordination lower than six), most of the Ge atoms are in pyra-

midal or defective octahedral geometry while a minority fraction of Ge atoms (e.g. about 30 % in Ref. [22]) are in tetrahedral geometries. The tetrahedral configuration is favored by homopolar Ge-Ge bonds [22, 24, 25] which are present in the liquid and survives in the amorphous phase due to fast quenching. The AD model generated in Ref. [21] by depositing about 600 atoms with thermal (300 K) kinetic energy features more Ge atoms in a tetrahedral bonding geometry (58 %) than those of a model with similar size generated by quenching from the melt (36 %) [21]. As expected, the larger fraction of tetrahedra is also related to the presence of a larger fraction of homopolar Ge-Ge bonds. The tetrahedral configurations are supposed to hamper the formation of crystalline nuclei since atoms in the crystal are all arranged in an octahedral bonding geometry. Although this is true below the glass transition which is of relevance for the data retention of the memory, it is unclear to which extent the tetrahedra present in the amorphous phase below T_g survive at the high temperature conditions of the set operation of the memory. DFT simulations of the supercooled liquid show that tetrahedra are clearly visible only below 600 K, [26] i.e. at temperatures lower than that corresponding to the maximum crystal growth velocity exploited in the memory [27]. Therefore, it is unclear whether the difference in the fraction of tetrahedral atoms reveled by the DFT simulations could be responsible for the differences in the crystallization kinetics of AD and MQ samples measured experimentally for GST.

Still, another argument was raised in favor of the existence of polyamorphism in GST. Since the bond lengths are shorter in the tetrahedral geometry than in the octahedral ones, a large fraction of tetrahedra in AD models could also reconcile the disagreement between the theoretical bond length in MQ models generated by DFT by different groups and the systematically shorter experimental bond lengths which, however, mostly refer to AD samples [21, 22, 23]. We quote, however, Ref. [28] for a different view on this issue. A different choice of the pseudopotential for Ge made in Ref. [28] lead to a higher fraction of Ge-Ge bonds in the DFT models of $Ge_2Sb_2Te_5$ which brought the bond lengths closer to experiments. A similarly higher fraction of Ge-Ge bonds and tetrahedra was found for amorphous GeTe in Ref. [29] where the same code and presumably the same Ge pseudopotential of Ref. [28] were used. An additional shortening in the bond lengths with a further increase in the fraction of tetrahedra and a better agreement with experiments was found in Ref. [29] by including the van der Waals corrections according to Grimme (D2) [30]. Note, however, that the fraction of tetrahedra in Ref. [29] is computed in a different manner with respect to the other DFT works mentioned above.

In the present work, we investigate the presence of polyamorphism in phase change materials by performing large scale molecular dynamics simulations of the deposition process. The resulting AD models allowed us to compare the crystallization kinetics of the AD and MQ amorphous phases. We focus here on the GeTe compound which shares many properties with the ternary GST alloys because of the availability of a machine learning interatomic potential that allows simulating several thousands of atoms for several ns. The interatomic potential for GeTe used here was generated by fitting a large database of DFT total energies of reference structures with a high-dimensional neural network (NN) scheme [31, 32] . The generation of AD models containing 8000 atoms also allowed us to largely improve the statistical accuracy in the analysis of the structural properties with respect to the relatively small 600-atom model used in the previous DFT work on GST [21]. The NN results confirm a difference in the fraction of tetrahedra between the AD and MQ models as found previously for

GST in Ref. [21]. This structural difference has, however, a little impact on the crystallization kinetics which turns out to be very similar in our AD and MQ models.

2 Computational details

Molecular dynamics (MD) simulations have been performed by using the NN interatomic potential for GeTe developed in Ref. [31, 32]. The potential was originally obtained in Ref. [31] by fitting a database of total energies obtained within DFT by means of the method introduced by Behler and Parrinello [33]. The database consists of the total energies of about 30000 configurations of 64-, 96-, and 216-atom supercells computed by employing the Perdew-Burke-Ernzerhof (PBE) exchange and correlation functional [34] and norm conserving pseudopotentials. The potential displays an accuracy close to that of the underlying DFT-PBE framework whose reliability in describing structural and dynamical properties of GeTe and other phase change materials has been validated in several previous works. [12, 13, 22, 23, 25] In order to deal with surfaces and nanowires, a new version of the potential was generated in Ref. [32] by enlarging the training set with about 5000 new configurations of crystalline and amorphous GeTe (a-GeTe) in a slab geometry (128-atom supercell) and about 7000 new configurations of crystalline, amorphous and liquid GeTe in a nanowire geometry (120- and 256-atom cells). We refer to the first version of the potential of Ref. [31] as NNP and to the second version of the potential of Ref. [32] as NNP2. The transferability of NNP and NNP2 was validated in previous works on the simulation of crystallization and thermal conductivity in the bulk and in nanowires and of the aging of the amorphous phase [35, 36, 37, 38, 39, 40].

The NNP2 reproduces the structural properties of crystalline GeTe slightly better than the previous NNP version of Ref. [31] (see additional material of Ref. [32]). Moreover, the generation of the amorphous phase by quenching from the melt in 100 ps by constant pressure molecular dynamics with NNP2 yields an equilibrium density at 300 K of 0.0315 atom/Å^3. This density is equal to the equilibrium density obtained by the DFT equation of state at zero temperature of a model initially generated by quenching from the melt in constant volume DFT-MD at the fixed experimental density of 0.03327 atom/Å^3 [31]. On the contrary, the equilibrium density of NNP [31] was 0.03351 atom/Å^3 which is closer to the experimental value of 0.03327 atom/Å^3 for AD a-GeTe,[41] although it is higher than the equilibrium density obtained by DFT as described above.

As we will see later, the crystal nucleation rate is strongly dependent on the density of the amorphous phase. Part of the simulations were then repeated by adding the van der Waals (vdW) correction according to Grimme (D2) by using the PBE parameters of Ref. [30] which yields an equilibrium density of the amorphous phase higher than that obtained by NNP2 alone and closer to the experimental value, as we will discuss in Sec. III. Since our previous simulations of the crystallization of bulk GeTe in Refs. [35, 36, 37, 39] did not include vdW interactions, for the sake of comparison with previous results, we report here on simulations of AD and MQ models that either include or neglect vdW interactions. MD simulations were performed with the NN code RuNNer [42] by using the DL_POLY code [43] as molecular dynamics driver. The time step was set to 2 fs, and temperature was controlled with a stochastic thermostat [44].

We generated AD and MQ models of GeTe to compare their structural properties and crystallization kinetics. As already mentioned, a typical technique for the growth of phase change materials is magnetron sputtering deposition. We emulated this process by depositing atoms with mean kinetic energy in the 1.5-10 eV range which is typical of magnetron sputtering

[45], although no detailed information on the actual energy distribution of atoms impinging on the surface are available in the literature for the deposition of phase change materials. First, we generated a 4000-atom bulk amorphous model by quenching from the melt in 100 ps (MQ model) at fixed density according to the protocol of Ref. [31]. This model was then used as an amorphous substrate for the growth of the AD amorphous phase. Since we did not know a priori what the resulting density of the AD models was, we chose as a substrate a MQ model at the density of 0.03351 atom/Å^3 close to the experimental one of the AD amorphous phase. The bulk model (MQ-high-ρ) was generated with a supercell of edges a = b = 62.0352 Å and c = 31.0176 Å with 3D periodic boundary conditions. After equilibration at 300 K, the bulk model was cut along the z direction to generate a slab with two free surfaces. The lower surface of the slab was frozen at the bulk positions while the upper surface was annealed at 380 K for 50 ps. The final model was then used as a substrate for the deposition of atoms that were inserted randomly (by keeping the overall GeTe stoichiometry) in a spatial region 5 Å thick at 30 Å over the upper surface of the substrate. We performed three different simulations with different average kinetic energy E_{ave} of the impinging atoms corresponding to 1.5, 5 and 10 eV that we refer to as AD-1.5, AD-5 and AD-10 in the following. We chose a Gaussian distribution of the kinetic energy with a variance equal to $E_{ave}/20$. This narrow distribution does not correspond to the typical energy distribution of deposited atoms in magnetron sputtering [46]. Nevertheless, by repeating the simulation for different E_{ave} we obtained detailed information on the dependence of the structure of the film on the energy of the majority of incoming particles. The orientation of the velocity of the impinging atoms is defined by the angles θ and ϕ in spherical coordinates with respect to the growth direction (z). The azimuthal angle θ was chosen randomly within a Gaussian distribution centered at zero with a variance of $2\pi/45$, i.e. a nearly vertical direction of the impinging atoms. The angle ϕ was chosen instead randomly with a uniform distribution in the range 0-2π.

The time interval between the deposition of two individual atoms must be sufficiently long to allow for the dissipation the kinetic energy transferred to the substrate. In the experimental deposition process, this energy dissipation occurs easily for a typical particle flux of about 10^{16} atom cm^{-2} s^{-1} which corresponds to a growth rate of 5 nm/s reported for phase change materials. [47] In the simulations, the time interval between the deposition of two atoms is set to 4 ps which corresponds to a particle flux of about 10^{24} atom cm^{-2} s^{-1} that is necessarily much larger than in experiments to reduce the computational cost. To prevent overheating of the surface, the temperature is controlled by properly thermostatting the system in the impact region and in the substrate region. The impact region extends from the surface down in the sample to a depth of 20 Å. The single deposition event consists of two steps: in the first 2 ps the substrate is thermostatted at 300 K while the impact region has no thermostat, in the subsequent 2 ps the thermostat is applied only to the impact region to bring the surface to the target temperature of 300 K. After the deposition of 100 atoms all the system is thermostatted at 300 K for 10 ps before starting a new bunch of depositions. We deposited a total number of 4000 atoms over the 4000-atom substrate.
The structural properties of the AD models have been analyzed by selecting a subsurface region 15 Å thick from 12 Å beneath the surface and extending in the bulk up to 7 Å above the substrate. This region contains about 2000 atoms. The structural properties have been computed at 300 K by averaging over a 30 ps trajectory. The distribution of ring size was computed by using the code *Atomes* [48] and the algorithm of Ref. [49]. For AD models, the distribution includes also the substrate.

In the simulation of crystallization, we used the "dot-product" bond order parameter Q_6 [50, 51] to identify a crystalline atom for the sake of comparison with our previous work [35] which we refer to for further details. We define an atom to be part of a crystalline region when its value of Q_6 is larger than the threshold of 0.45 which was shown in Ref. [35] to discriminate well between the amorphous/liquid and crystalline environments.

3 Results

3.1 Structural properties of as-deposited amorphous GeTe

We first discuss the results of simulations with the NNP2 without vdW corrections. Three snapshots of the deposition process of model AD-5 are shown in Fig. 1.

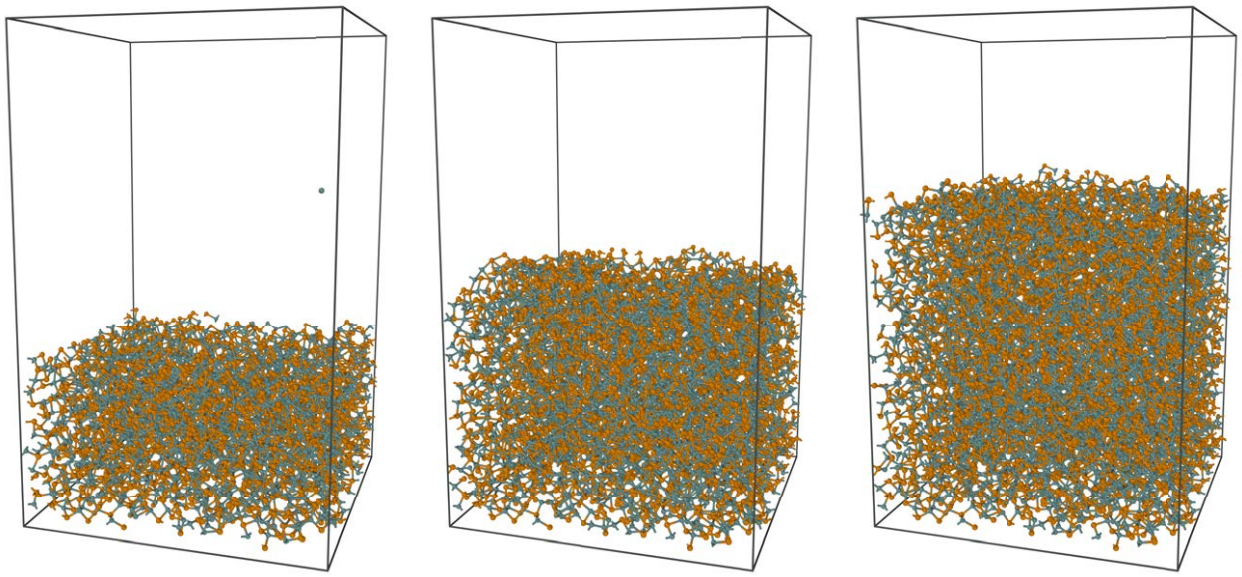

(a) (b) (c)

Figure 1: Snapshots of deposition process with impinging atoms with 5 eV kinetic energy. a) 4000-atom model of the amorphous substrate, b) the growing model after the deposition of 2000 atoms, c) the final model after deposition of 4000 atoms.

The structural properties of the film are weakly dependent on the kinetic energy of the deposited atoms in the range 1.5-5-10 eV as we will detail later. On the contrary, a very different morphology is obtained by depositing atoms with thermal energy of 25 meV, a snapshot of this latter model is shown in Fig. S1 in the Supporting Information (SI). The resulting density of the film is very low (0.0252 atom/Å^3) compared to the equilibrium density of the MQ model (0.0315 atom/Å^3) with the formation of a columnar structure and voids. The density of the AD film is measured in the region from 12 Å below the surface to 7 Å above the substrate which is representative of the bulk-like region of the deposited film. The resulting density of the models AD-1.5, AD-5, and AD-10 are 0.0321, 0.03183 and 0.03161 atom/Å^3, respectively, which is very close to the equilibrium density of the MQ model (0.0315 atom/Å^3, with no vdW interactions). The density of the substrate decreases from the initial density of 0.03351 atom/Å^3 to a value close to that of the growing film. The local density as a function of the depth in the film is shown in Fig. S2 in the SI. The very different morphology of the film deposited with 25 meV energy atoms suggests that surface mobility is crucial for the growth of a dense and homogeneous film. This outcome might partially result from the very high deposition rate that we have chosen due to computational constraints. By reducing the deposition rate, deposited atoms might have more time to diffuse on the surface before the thermal spike fades away. On the other hand, the fact that the structural properties of our films do not change significantly by changing the kinetic energy of the impinging atoms from 1.5 eV to 10 eV at the same fixed deposition rate suggests that surface diffusivity is ac-

counted for sufficiently well by our simulations with high energy atoms, otherwise we would have expected a different morphology with the much hotter 10 eV energy atoms than with atoms at 1.5 eV.

The structural properties of the three films (AD-1.5, AD-5, AD-10 models) at 300 K are analyzed in terms of the pair correlation functions (Fig. 2a), distribution of coordination numbers (Fig. S3 in the SI), average partial coordination numbers (Table 1) and bond angle distribution function (Fig. S4 in the SI). The coordination numbers are obtained by integrating the partial pair correlation functions up to the bonding cutoff of 3.00 Å for Ge-Ge and Te-Te bonds and 3.22 Å for Ge-Te bonds. The same cutoff is used also in the analysis of the models generated by adding the vdW interactions that we will discuss later. The structural properties mentioned above change very slightly among the three AD models which means that the morphology of the film is not dependent on the energy of the impinging atoms in the range 1.5-10 eV. The AD models differ very slightly also from the MQ model, but for the fraction of Ge-Ge bonds (see Ge-Ge partial correlation function in Fig. 2 and the Ge-Ge partial coordination number in Table 1) that it is larger in the AD films.

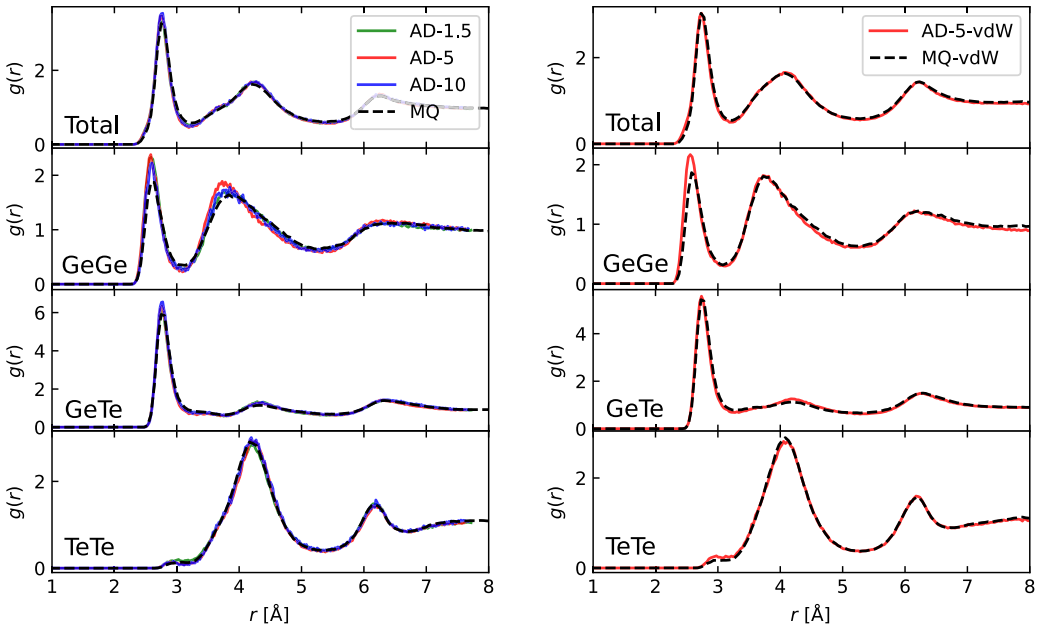

(a) (b)

Figure 2: a) Partial and total pair correlation functions of deposited films AD-1.5, AD-5, AD-10 models corresponding to different average kinetic energy of the deposited atoms compared with the data for the MQ model at the theoretical equilibrium density (see text). b) Partial and total pair correlation functions of the deposited AD-5-vdW model generated with an average kinetic energy of the deposited atoms of 5 eV, compared with the data for the MQ-vdW model quenched from the melt at the same atomic density of the AD-5-vdW model (see text). Both the AD-5-vdW and MQ-vdW models are generated by adding vdW interactions (see text).

The larger fraction of Ge-Ge bonds in the AD models is responsible for a larger fraction of tetrahedral Ge atoms [24, 25] with respect to the MQ model as it can also be inferred from the angle distribution functions in Fig. S4 in SI. The peak at about 90^o for Ge atoms are due to pyramidal and defective octahedral configurations while the weak peak at about 170 ^{o} are

Table 1: Average partial coordination numbers for the AD-1.5, AD-5, AD-10 models compared with the data for the MQ model at the theoretical equilibrium density (see text). The AD-5-vdW and MQ-vdW data refer to the models generated by including vdW interactions (see text). The MQ-high-ρ data refers to the model at the density close to the experimental value without vdW interactions (see text).

		MQ	AD-1.5	AD-5	AD-10	MQ-vdW	AD-5-vdW	MQ-high-ρ
Ge	with Ge	0.925	1.061	0.996	0.937	0.979	1.101	0.883
	with Te	2.971	2.885	2.910	2.963	2.991	2.888	3.136
	totale	3.895	3.946	3.906	3.900	3.970	3.989	4.019
Te	with Ge	2.971	2.885	2.900	2.900	2.991	2.853	3.136
	with Te	0.040	0.059	0.049	0.047	0.058	0.090	0.030
	total	3.011	2.945	2.949	2.947	3.049	2.943	3.166

due to axial bonds in a defective octahedral configuration. The shoulder at about 109^o due to tetrahedra is slightly more evident in the AD models than in the MQ one (Fig. S4 in SI). A quantitative measure of the fraction of tetrahedral environments can be obtained from the local order parameter q introduced in Ref. [52]. It is defined as $q = 1 - \frac{3}{8}\sum_{i>k}(\frac{1}{3} + \cos\theta_{ijk})^2$, where the sum runs over the pairs of atoms bonded to a central atom j and forming a bonding angle θ_{ijk}.The order parameter evaluates to q=1 for the ideal tetrahedral geometry, to q=0 for the 6-fold coordinated octahedral site, to q=5/8 for a 4-fold coordinated defective octahedral site, and q=7/8 for a pyramidal geometry (three bonding angles of 90°). The distribution of the q order parameters for the AD and MQ models are compared in Fig. 3a. As discussed in previous works, [22, 53, 54] the fraction of Ge atoms in tetrahedral environments can be quantified by counting the 4-fold coordinated atoms with q in the range $0.8 < q < 1$. The resulting fraction of Ge atoms in tetrahedral geometry (with respect to the total number of Ge atoms) is reported in Table 2 for the different AD and MQ models. The distribution of the different types of tetrahedra (isolated, corner- or edge-sharing) are also shown in Table 2. The fraction of tetrahedra in the AD models falls in the range 45-48 % which is larger than the value of 39 % of the MQ model. This result is in qualitative agreement with the DFT simulations of GST in Ref. [21] which yielded a fraction of tetrahedra of 58 % and 36 % in the AD and MQ models. One should consider that the thickness of the deposited GST film in the DFT simulation of Ref. [21] is relatively thin with respect to our AD models. The average fraction of tetrahedra given above for our models is computed starting from 12 Å beneath the surface. Closer to the surface the fraction of tetrahedra raises up to 55 % which is closer to the DFT value of 58 % for GST of Ref. [21]. This is shown in Fig. S5 in SI where the fraction of tetrahedra, averaged over thin slices perpendicular to the growth direction, is reported as a function of the distance from the surface.

As we will in Sec. 3.2 the difference in the fraction of tetrahedra between the AD and MQ model does not lead to a sizeable difference in the kinetics of crystal nucleation and growth. To address other possible features affecting the crystallization kinetics, such as the density, we generated an AD model by adding the vdW interaction à la Grimme which, as discussed in Sec. 2, leads to a higher equilibrium density of the amorphous phase. Since, as we have above, the structural properties of the AD films do not depend on the energy of the deposited atoms in the range 1.5-10 eV, we generated a single AD model with vdW interactions just for the intermediate energy of the impinging atoms of 5 eV. The density of the resulting AD

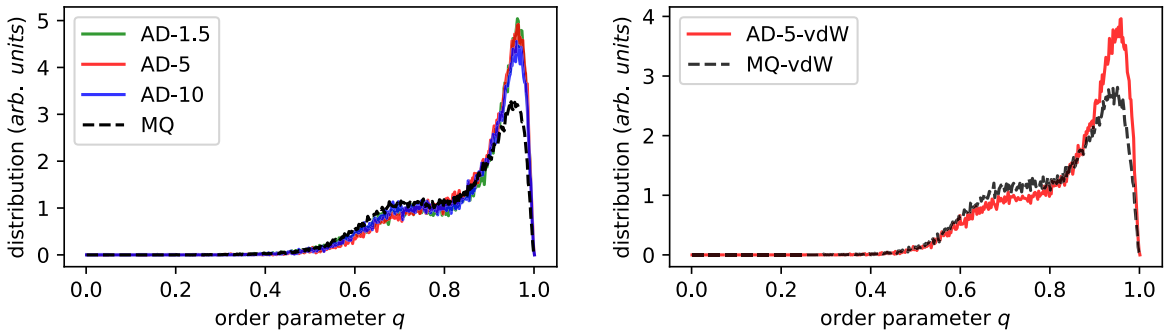

(a) (b)

Figure 3: a) Distribution of the q order parameter for tetrahedricity of the 4-fold coordinated Ge atoms in the AD-1.5, AD-5, AD-10 models, compared with the data for the MQ model at the theoretical equilibrium density (see text). b) Distribution of the q order parameter of the 4-fold coordinated Ge atoms in the deposited AD-5-vdW model generated with an average kinetic energy of the deposited atoms of 5 eV, compared with the data for the MQ-vdW model quenched from the melt at the same atomic density of the AD-5-vdW model (see text). Both AD-5-vdW and MQ-vdW are generated by adding vdW interactions (see text). The peak close to 1 is due to the tetrahedral geometry while the peak close to 0.625 is due to defective octahedral geometries.

Table 2: Percentage of Ge atoms in tetrahedral environments and fraction of tetrahedra in isolated, corner- and edge-sharing configurations for the AD-1.5, AD-5, AD-10 models compared with the data for the MQ model at the theoretical equilibrium density (see text). The AD-5-vdW and MQ-vdW data refer to the models generated by including vdW interactions (see text). The MQ-high-ρ data refers to the model at the density close to the experimental value without vdW interactions (see text).

	MQ	AD-1.5	AD-5	AD-10	MQ-vdW	AD-5-vdW	MQ-high-ρ
Tetraedra fraction (%)	39	46	48	45	37	44	34
Isolated (%)	7	7	7	8	8	8	10
Corner-sharing (%)	75	78	76	73	79	81	75
Edge-sharing (%)	18	15	17	19	13	11	15
Face-sharing (%)	0	0	0	0	0	0	0

model, named hereafter AD-5-vdW, of 0.0346 atom/Å^3 is higher than the value of about 0.0315 atom/Å^3 of the AD (and MQ) models generated without vdW interactions. The experimental value for a-GeTe of 0.03327 atom/Å^3 is midway between the density of the models generated with and without vdW interactions (about ± 5 %). The structural properties of the AD-5-vdW model are compared with those of a model quenched from the melt at the same density of 0.0346 atom/Å^3 (MQ-vdW) in Figs. 2b (pair correlation functions) and 3b (q order parameter) and Figs. S6-S7 in the SI (coordination numbers and bond angles distributions). The average coordination numbers, the fraction of tetrahedral Ge atoms and the fraction of the different types of tetrahedra are reported instead in Tables 1 and 2. The comparison between AD-5-vdW and MQ-vdW models is overall very similar to the analysis reported above for the models generated without vdW interactions which also means that the difference between AD and MQ models are only slightly dependent on the density. In particular, the fraction of tetrahedra in the as-deposited AD-5-vdW model is 44 % as compared to a value of 37 % for the MQ-vdW model, similarly to the results obtained without vdW interactions. In spite of a moderately different fraction of tetrahedra, the crystallization kinetics is very similar for the AD and MQ samples as we will discuss in the next section.

3.2 Crystallization kinetics of as-deposited amorphous GeTe

The crystallization of MQ amorphous GeTe was studied by large scale simulations with the NNP and NNP2 in our previous works.[32, 35, 36, 39] Before discussing the crystallization of the AD models, we briefly summarize the results of our previous works. We previously simulated the homogeneous crystallization of the supercooled liquid at different temperatures,[35] the crystal growth in a slab model with an interface between the crystal and the supercooled liquid, [36] and the homogenous crystallization of an amorphous model heated above the glass transition temperature.[39] In all these simulations we used the NNP of Ref. [31] that, as we mentioned in Sec. II, yielded a theoretical equilibrium density of 0.03351 atom/Å^3 which is very close to the experimental value for a-GeTe (0.03327 atom/Å^3 from Ref. [41]) and for the liquid at the melting temperature T_m= 998 K (0.0334 atom/Å^3 from Ref. [55]). The NNP theoretical equilibrium density of a-GeTe is, however, higher that the theoretical equilibrium density obtained within the DFT framework (0.0315 atom/Å^3 from Ref. [31]) from which the training database was built. The better agreement with experiment of the NNP result with respect to the DFT ones is, therefore, fortuitous. Anyway, the NNP simulations of crystallization of GeTe in Refs. [35, 36, 39] were performed at a fixed density of 0.03327 atom/Å^3. In the homogeneous crystallization of the supercooled liquid at this density (4000-atom supercell) we observed two different regimes. At temperatures below 600 K several nuclei appeared on the time scale of few hundreds of ps, while at temperatures in the range 600–675 K a single overcritical nucleus appeared after an incubation time up to 350 ps long. Above 675 K, we did not observe crystallization over 2 ns due to the decrease of the nucleation rate by approaching T_m.[35] The simulations also provided a quantitative evaluation of the crystal growth velocity which amounts to 0.45-6.2 m/s in the temperature range 500-675 K that validated the application of the classical nucleation theory (Wilson-Frenkel formula for crystal growth velocity [56]).[35] Moreover, the simulation of crystallization of the amorphous phase overheated in the same temperature range yielded crystal growth velocities similar, albeit slightly lower, than those obtained for the supercooled liquid (see Table 1 in Ref. [39]). Since in PCM the supercooled liquid is embedded in a crystalline matrix, its density is expected to fall within the equilibrium density of the crystal and that of the liquid. Because of this, the effect of pressure on the crystallization kinetics was evaluated in Ref. [35] with the

NNP [31] by repeating the simulation of the homogenous crystallization at the higher density of 0.0357 atom/Å^3 corresponding to the theoretical density of the crystal. At this higher density, we observed a reduction in the crystal growth velocity by about a factor two with respect to those obtained at the density of the amorphous phase. A change in the incubation time by increasing density was not documented in Ref. [35], but anyway it must be limited to a fraction of ns. Crystal growth at the crystal/liquid rim was simulated instead in Ref. [36] with the NNP [31] and in Ref. [32] with the NNP2 devised there to address the crystallization of a GeTe nanowire. As already stated in Sec. II, the same NNP2 suitable to describe surfaces and nanoparticle is used in the present simulations of the AD and MQ models. We also highlighted previously in Sec. II that the NNP2 provides a theoretical equilibrium density of MQ a-GeTe equal to the DFT one (0.0315 atom/Å^3) but lower than the experimental one (0.03327 atom/Å^3). However, the simulations in Ref. [32] with the NNP2 were performed at the experimental density of the liquid which is very close to the density chosen for the simulation with the NNP in Ref. [36]. As a consequence the crystal growth velocities obtained in Refs. [36] and [32] are very similar.

The dependence of crystal nucleation on the density of a-GeTe was analyzed in a more recent paper by another group [57] where a different NN potential was developed. It was shown that the incubation time for nucleation is strongly dependent on the ability of the NN potential in describing the energy difference between flat and puckered 4-membered rings. It is known that the formation and reorientation of 4-membered rings play a crucial role in the crystal nucleation,[2, 11] as these are the building blocks of the crystalline phase. The energy barrier for the transformation from a puckered to a flat 4-membered rings is therefore expected to control the nucleation rate. In Ref. [57] it was shown indeed that a revised NN potential fitted on a training set which includes information on such an energy barrier leads to incubation times for nucleation of about 7 ns and 17 ns (at a density of 0.0337 atom/Å^3) in two different runs at 500 K with respect to a value of a few hundreds of ps reported in our previous work [35]. Nucleation was not observed instead over 20 ns at temperatures in the range 550-650 K. [57] Moreover, it was also shown that by increasing the density to 0.0361 atom/Å^3 the incubation time decreases to a fraction of ns at 500 K and to less than 3 ns in the temperature range 550-650 K.[57]

The strong dependence of the incubation time for nucleation on atomic density highlighted in Ref. [57] is confirmed by our simulations. The fraction of a crystalline atoms as a function of time (see Sec. II for definition) is reported in Fig. 4 for two MQ models at 600 K at different densities: i) the higher density of ρ=0.03351 atom/Å^3, used in our previous works (MQ-high-ρ),[32, 35, 36, 39] and close to the experimental value, and ii) the theoretical equilibrium density of the NNP2 melt-quenched model of 0.0315 atom/Å^3 (MQ). At the higher density (MQ-high-ρ) an incubation time of a fraction of ns is observed above which several fast growing nuclei appear, while at the lower density (MQ) an overcritical nucleus appears only after about 3.5 ns. A similar behavior is observed in asdep model (AD-5) annealed at 600 K which features a density (ρ= 0.03183 atom/Å^3, see Sec. 3.1) close to that of the MQ model. A sequence of snapshots of the simulation of the AD-5 model is reported in Fig. S8 in the SI. Nucleation and growth on the time scale of a few ns is observed also at the lower temperatures of 550 K (Fig. S9 in SI) and 500 K (Fig. S10 in SI). The total number of crystalline atoms as a function of time is reported for the MQ and AD-5 models at 600 K in Fig. S11 and for the AD-5 model at different temperatures in Fig. S12. Just a single overcritical nucleus is ob-

served in the MQ model at 600 K and in the AD-5 model at 500 K and 600 K while two nuclei appear in the AD-5 model at 550 K in the time span of 5 ns. Overcritical nuclei form in the bottom part of the slab at 600 K and 500 K, but also at the surface at 550 K. As mentioned above, 4-membered rings were shown in previous works to play a crucial role in the crystallization kinetic. The distribution of rings length for MQ models at different densities are compared in Fig. S13 in SI with those of the AD-5 model at 300 and 600 K before crystal nucleation takes place. As expected, a larger fraction of tetrahedra results in a lower fraction of 4-membered rings, although the differences are rather tiny for our models.

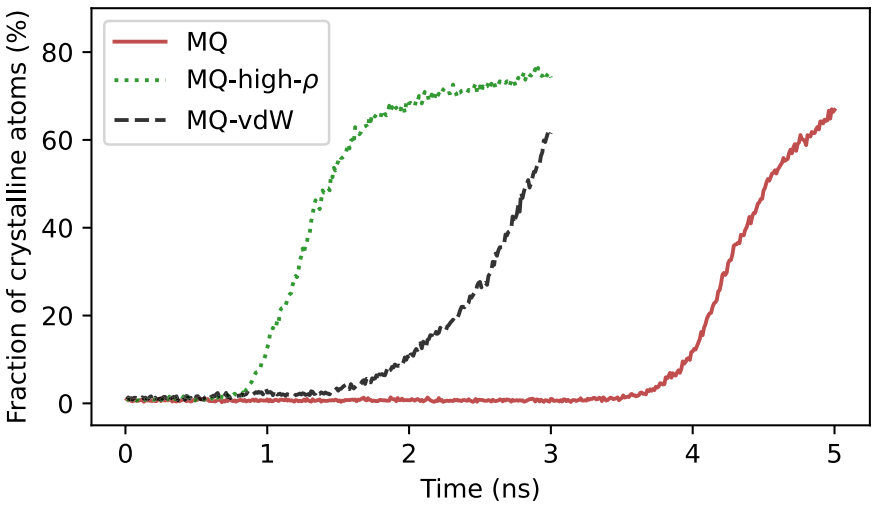

Figure 4: Evolution in time of the fraction of crystalline atoms (4000-atom cell) during the crystallization at 600 K of melt-quenched models of a-GeTe at different densities. The crystalline atoms are identified by the Q_6 bond order parameter (see Sec. II). The curve labelled MQ-high-ρ refers to a model at the higher density of ρ=0.03351 atom/Å^3 equal to that used in our previous works [32, 35, 36, 39] and close to the experimental value. The curve labelled MQ refers to the lower density of 0.03183 atom/Å^3 which corresponds to the theoretical equilibrium density of a-GeTe generated by quenching from the melt in a constant pressure simulation. The curve labelled MQ-vdW refers to simulations with vdW interactions at ρ=0.0346 atom/Å^3 (MQ-vdW) corresponding to the density of the AD films generated by adding vdW interactions. Only the simulations of the latter MQ-vdW model includes vdW interactions.

Still, no difference between AD and MQ models arose so far on the crystallization kinetics. However, since the nucleation rate is strongly dependent on the density, we repeated the simulation of crystallization of the MQ-vdW and AD-5-vdW models which feature a density (see Sec. 3.1) closer to the experimental one. The fraction of crystalline atom of the MQ-vdW is shown in Fig. 4 for comparison with the other MQ models at different densities. As expected, the MQ-vdW model crystallizes faster than the MQ model at lower density. The incubation time of the MQ-vdW model of about 0.9 ns is longer than that of the MQ-high-ρ model (see Fig. 4), despite its higher density, possibly because of a decrease of the atomic mobility due to the vdW interaction which was documented in previous works [55]. The total number of crystalline atoms as a function of time at 600 K for the MQ-vdW and AD-5-vdW models is then compared in Fig. 5. Both models feature a similar incubation time and a similar crystal growth velocity. In the AD-5-vdW model up to four different overcritical nuclei form, two in the bulk and two closer to the surface, while a single overcritical nucleus is growing in the MQ-vdW model. Since the AD model is twice the size of the MQ model, the

incubation time per unit volume is even shorter for the AD than for the MQ model. Snapshots of the crystallization at different times are shown in Fig. 6 for the AD-5-vdW and, for the sake of comparison, in Fig. S14 in SI for the MQ-vdW model.

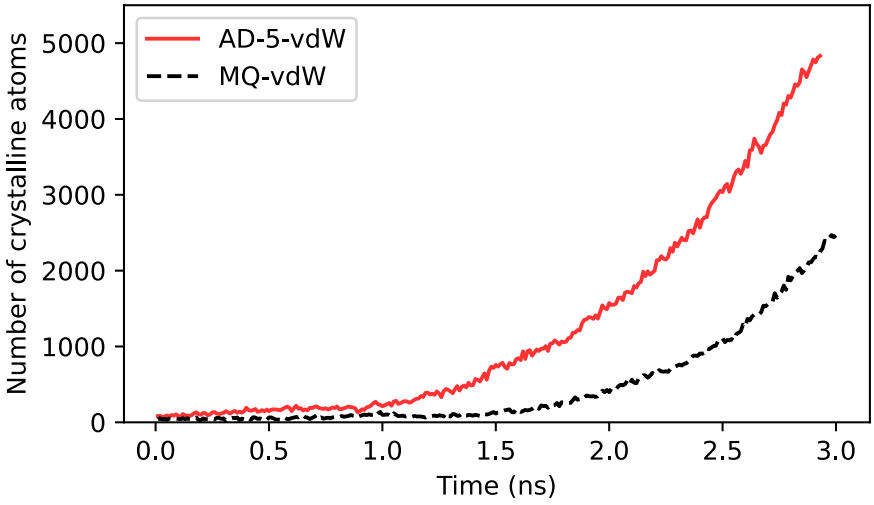

Figure 5: Evolution in time of the number of crystalline atoms during the crystallization at 600 K of the melt-quenched MQ-vdW (4000 atoms) and asdep AD-5-vdW models (8000 atoms) generated by including vdW interactions. The density of the MQ-vdW is the same of the density of the AD-5-vdW model in the deposited region (see text). A single nucleus grows in the MQ-vdW model while up to four overcritical nuclei form in the AD-5-vdW model.

In summary, no clear differences in the crystallization kinetics are detected neither between the AD-5-vdW and MQ-vdW models generated with vdW interactions on a time scale sufficiently long for both models to crystallize. Although a slightly different fraction of Ge in tetrahedral configurations is found in the melt-quenched and as-deposited models, these structural differences do not seem sufficient to affect the crystallization kinetics at least at the high temperature (600 K) conditions investigated here. On the other hand, experimentally the crystallization kinetics is faster in MQ than in AD samples, although the difference is less striking in GeTe than in GST. We can reconcile our results with experiments by ascribing the faster crystallization of MQ samples observed experimentally to the presence of a non-equilibrium population of subcritical crystallites formed during the quenching from the melt which reduce the incubation time as proposed in Ref. [16, 19, 20]. We do not see this pre-formed nuclei neither in our MQ model, possibly because of a very fast quenching from the melt (100 ps) and of the limited size of the simulation cell. However, a pre-formed population of subcritical nuclei should be important during crystallization at lower temperatures at which the nucleation rate is low than at the temperatures considered here . An overestimation of the nucleation rate itself is also possible due to limitations of our NN potentials (a too low barrier from puckered to flat 4-membered rings) as pointed out in Ref. [57]. In spite of these uncertainties, our results seem to reliably suggest that the difference in the fraction of tetrahedra is not the key to justify the difference in the crystallization kinetics of AD and MQ samples.

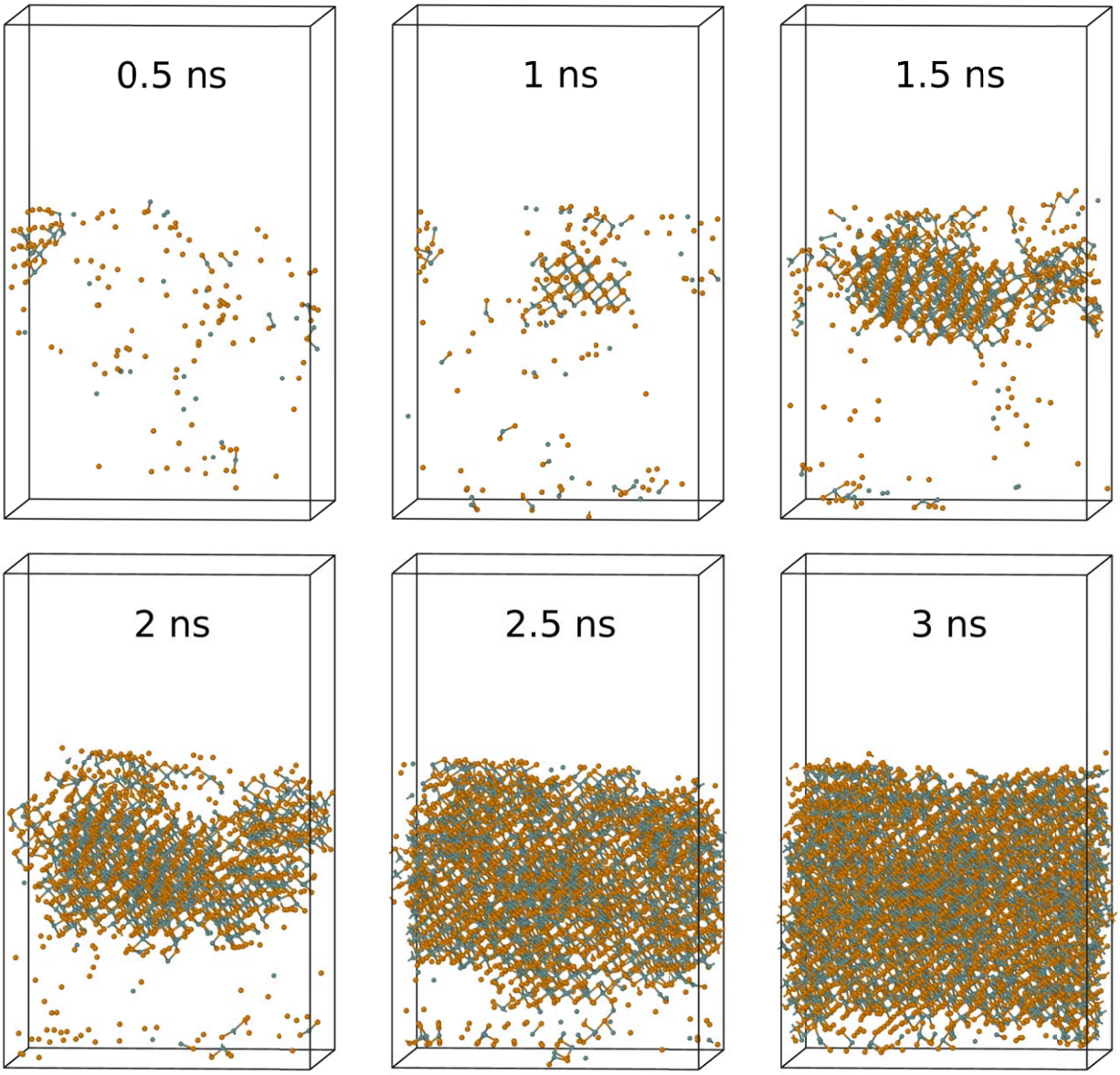

Figure 6: Snapshots of the crystalline atoms identified by the bond order parameter Q_6 (see Sec. II) in the simulations of the AD-5-vdW model at 600 K at different times. The bottom part is the substrate while the upper part is the free surface.

4 Conclusions

In summary, we have generated models of AD a-GeTe by molecular dynamics simulations mimicking the growth conditions of magnetron sputtering deposition. The NN interatomic potential generated previously for GeTe has been used. [32, 21] Three different simulations have been performed with an average kinetic energy of the impinging atoms of 1.5, 5 and 10 eV. The structure of the deposited film is very similar for all the three simulations with a density close to the equilibrium density of the amorphous phase generated by quenching from the melt in NPT simulations. On the contrary, the film obtained by depositing atoms with a thermal kinetic energy of 25 meV has a much lower density and a porous columnar structure which is inconsistent with the density of the films measured experimentally. The structural properties of the films deposited with kinetic energy in the range 1.5-10 eV are overall very similar with that of the melt quenched amorphous phase, but for a slightly larger fraction of Ge atoms in a tetrahedral geometry and for a larger fraction of homopolar Ge-Ge bonds in agreement with previous DFT results on GST [21]. The fraction of tetrahedra is further enhanced close to the surface of the deposited film. However, these structural differences do not lead to sizable changes in the crystallization kinetics of the AD and MQ models on the time scale of a few ns at 600 K. This is true either by including or neglecting vdW interactions in the interatomic potential. We would then confirm that the difference in the crystallization kinetics observed experimentally between the AD and MQ phases (although less striking for GeTe than for GST for instance) should not be due to an intrinsic polyamorphism but to the presence of a pre-formed crystalline nuclei as suggested in previous works [16] and observed experimentally by fluctuation TEM [19, 20].

Supporting Information
Supporting Information is available from the Wiley Online Library.

Acknowledgments
This work was partially funded by the European Union's Horizon 2020 research and innovation programme under Grant Agreement No. 824957 (BeforeHand: Boosting Performance of Phase Change Devices by Hetero- and Nanostructure Material Design) and by the PRIN research grant "NEuroMorPHic devices bASed on chalcogenIde heteroStructures", No. 20203K2T7F funded by the Italian Ministry of University and Research (MUR)".

Conflict of Interest
The authors declare no conflict of interest.

Data Availability Statement
The data that support the findings of this study are available from the corresponding author upon reasonable request.

References

[1] M. Wuttig, N. Yamada, *Nat. Mater.* **2007**, *6,* 824.

[2] W. Zhang, R. Mazzarello, M. Wuttig, E. Ma, *Nat. Rev. Mater.* **2019**, *4,* 150.

[3] P. Noé, C. Vallée, F. Hippert, F. Fillot, J.-Y. Raty, *Semicond. Sci. Technol.* **2018**, *33*, 1 013002.

[4] P. Cappelletti, R. Annunziata, F. Arnaud, F. Disegni, A. Maurelli, P. Zuliani, *J. Phys. D Appl. Phys.* **2020**, *53,* 193002.

[5] P. Fantini, *J. Phys. D: Appl. Phys.* **2020**, *53,* 283002.

[6] S. W. Fong, C. M. Neumann, H.-S. P. Wong, *IEEE Trans. Electron. Dev.* **2017**, *64,* 4374.

[7] M. Wuttig, H. Bhaskaran, T. Taubner, *Nat. Photonics* **2017**, *11*, 8 465.

[8] J. Feldmann, N. Youngblood, M. Karpov, H. Gehring, X. Li, M. Stappers, M. Le Gallo, X. Fu, A. Lukashchuk, A. Raja, J. Liu, C. D. Wright, A. Sebastian, T. J. Kippenberg, W. H. P. Pernice, H. Bhaskaran, *Nature* **2021**, *52,* 589.

[9] B. J. Shastri, A. N. Tait, T. Ferreira de Lima, W. H. P. Pernice, C. D. Bhaskaran, H. Wright, P. R. Prucnal, *Nat. Photonics* **2021**, *15,* 102.

[10] A. Sebastian, M. Le Gallo, R. Khaddam-Aljameh, E. Eleftheriou, *Nat. Nanotechnol.* **2020**, *15,* 529.

[11] J. Hegedüs, S. R. Elliott, *Nat. Mater.* **2008**, *7,* 399.

[12] Y. Xu, Y. Zhou, X.-D. Wang, W. Zhang, E. Ma, V. L. Deringer, R. Mazzarello, *Adv. Mater.* **2022**, *34,* 2109139.

[13] J. Kalikka, J. Akola, R. O. Jones, *Phys. Rev. B* **2016**, *94,* 134105.

[14] R. Lotnyk, M. Behrens, B. Rauschenbach, *Nanoscale Adv.* **2019**, *1,* 3836.

[15] L. van Pieterson, M. H. R. Lankhorst, M. van Schijndel, A. E. T. Kuiper, J. H. J. Roosen, *J. Appl. Phys.* **2005**, *97,* 083520.

[16] V. Weidenhof, I. Friedrich, S. Ziegler, S. Wuttig, *J. Appl. Phys.* **2001**, *89,* 3168.

[17] S. Raoux, H.-Y. Cheng, B. Munoz, J. Jordan-Sweet, *Proc. E/PCOS 2009* **accessed August 2022**, *https://www.epcos.org/_files/ugd/3d44dd_22788a7f40884493a429165fd27a636e.pdf.*

[18] B. J. Kooi, M. Wuttig, *Adv. Mater.* **2020**, *32,* 1908302.

[19] B.-S. Lee, R. M. Shelby, S. Raoux, C. T. Retter, G. W. Burr, S. N. Bogle, K. Darmawikarta, S. G. Bishop, J. R. Abelson, *J. Appl. Phys.* **2014**, *115,* 063506.

[20] B.-S. Lee, K. Darmawikarta, S. Raoux, R. M. Shelby, S. Raoux, Y.-H. Shih, Y. Zhu, S. G. Bishop, J. R. Abelson, *Appl. Phys. Lett.* **2014**, *104,* 071907.

[21] J. Akola, J. Larrucea, R. O. Jones, *Phys. Rev. B* **2011**, *83,* 094113.

[22] S. Caravati, M. Bernasconi, T. D. Kuehne, M. Krack, M. Parrinello, *Appl. Phys. Lett.* **2007**, *91* 171906.

[23] J. Akola, R. O. Jones, *Phys. Rev. B* **2007**, *76,* 235201.

[24] V. L. Deringer, W. Zhang, M. Lumeij, S. Maintz, M. Wuttig, R. Mazzarello, R. Dronskowski, *Angew. Chem. Int. Ed.* **2014**, *53,* 10817.

[25] R. Mazzarello, S. Caravati, S. Angioletti-Uberti, M. Bernasconi, M. Parrinello, *Phys. Rev. Lett.* **2010**, *104,* 085503.

[26] M. Cobelli, D. Dragoni, S. Caravati, M. Bernasconi, *Phys. Rev. Mat.* **2021**, *5,* 045004.

[27] J. Orava, A. L. Greer, B. Gholipour, D. W. Hewak, C. E. Smith, *Nat. Mat.* **2012**, *11,* 279.

[28] A. Bouzid, G. Ori, M. Boero, E. Lampin, C. Massobrio, *Phys. Rev. B* **2017**, *96,* 224204.

[29] M. Micoulaut, A. Piarristeguy, H. Flores-Ruiz, A. Pradel, *Phys. Rev. B* **2017**, *96,* 184204.

[30] S. Grimme, *J. Chem. Phys.* **2006**, *27,* 1787.

[31] G. C. Sosso, G. Miceli, S. Caravati, J. Behler, M. Bernasconi, *Phys. Rev. B* **2012**, *85,* 174103.

[32] S. Gabardi, E. Baldi, E. Bosoni, D. Campi, S. Caravati, G. C. Sosso, J. Behler, M. Bernasconi, *J. Phys. Chem C* **2017**, *121,* 23827.

[33] J. Behler, M. Parrinello, *Phys. Rev. Lett.* **2007**, *98,* 146401.

[34] J. P. Perdew, K. Burke, M. Ernzerhof, *Phys. Rev. Lett.* **1996**, *77,* 3865.

[35] G. C. Sosso, G. Miceli, S. Caravati, F. Giberti, J. Behler, M. Bernasconi, *J. Phys. Chem. Lett.* **2013**, *4,* 4241.

[36] G. C. Sosso, M. Salvalaglio, J. Behler, M. Bernasconi, M. Parrinello, *J. Phys. Chem. C* **2015**, *119,* 6434.

[37] S. Gabardi, S. Caravati, G. C. Sosso, J. Behler, M. Bernasconi, *Phys. Rev. B* **2015**, *92,* 054201.

[38] G. C. Sosso, D. Donadio, S. Caravati, J. Behler, M. Bernasconi, *Phys. Rev. B* **2012**, *86,* 104301.

[39] S. Gabardi, G. C. Sosso, J. Behler, M. Bernasconi, *Faraday Discuss.* **2019**, *213,* 287.

[40] E. Bosoni, D. Campi, D. Donadio, G. C. Sosso, J. Behler, M. Bernasconi, *J. Phys. D: Appl. Phys.* **2020**, *53,* 054001.

[41] G. E. Ghezzi, J. Y. Raty, S. Maitrejean, A. Roule, E. Elkaim, F. Hippert, *Appl. Phys. Lett.* **2011**, *99,* 151906.

[42] J. Behler, *RuNNer: A Neural Network Code for High- Dimensional Potential-Energy Surfaces* (Germany: Institut für Physikalische Chemie, Universität Göttingen).

[43] W. Smith, T. R. Forester, *J. Mol. Graph.* **1996**, *14,* 136.

[44] G. Bussi, D. Donadio, M. Parrinello, *J. Chem. Phys.* **2017**, *126,* 014101.

[45] P. Brault, E. C. Neyts, *Catalysis Today* **2015**, *256,* 3.

[46] K. Meyer, I. K. Schuller, C. M. Falco, *J. Chem. Phys.* **1981**, *52,* 5803.

[47] I. Friedrich, V. Weidenhof, S. Lenk, M. Wuttig, *Thin Solid Films* **2001**, *389,* 239.

[48] Code *Atomes*, *https://atomes.ipcms.fr,* **2022**.

[49] S. Le Roux, P. Jund, *Comp. Mater. Sci.* **2010**, *49,* 70.

[50] P. J. Steinhardt, D. R. Nelson, M. Ronchetti, *Phys. Rev. B* **1983**, *28,* 784.

[51] J. S. van Duijneveldt, D. Frenkel, *J. Chem. Phys.* **1992**, *96,* 4655.

[52] J. R. Errington, P. G. Debenedetti, *Nature* **2001**, *409,* 318.

[53] E. Spreafico, S. Caravati, M. Bernasconi, *Phys. Rev. B* **2011**, *84,* 144205.

[54] G. C. Sosso, S. Caravati, M. Mazzarello, R. Bernasconi, *Phys. Rev. B* **2011**, *83,* 134201.

[55] H. Weber, M. Schumacher, P. Jóvári, Y. Tsuchiya, W. Skrotzki, R. Mazzarello, I. Kaban, *Phys. Rev. B* **2017**, *96,* 054204.

[56] H. A. Wilson, *Philos. Mag.* **1900**, *50,* 237.

[57] D. Lee, K. Lee, D. Yoo, W. Jeong, S. Han, *Comp. Mat. Sci.* **2020**, *181,* 109725.